



# An EBSD Study on the Stability of Retained Austenite in Low-Si TRIP Steels During Uniaxial Tension

FAYEZ AL-HARBI,<sup>1,2,3</sup> AZDIAR A. GAZDER,<sup>2</sup>  
and ELENA PERELOMA<sup>1,2,4</sup>

1.—School of Mechanical, Materials, Mechatronic and Biomedical Engineering, University of Wollongong, Wollongong, NSW 2522, Australia. 2.—Electron Microscopy Centre, University of Wollongong, Wollongong, NSW 2522, Australia. 3.—*Present address:* Saudi Basic Industries Corporation (SABIC), Riyadh, Saudi Arabia. 4.—e-mail: elenap@uow.edu.au

Two transformation-induced plasticity steels, with and without Nb–Ti additions, were subjected to uniaxial tension after simulated thermo-mechanical processing. Electron back-scattering diffraction, with phase segmentation implemented during post-processing, was used to investigate the stability of retained austenite (RA) by analyzing its size, morphology, and neighboring phases. The rate of RA transformation to martensite was higher in the Nb–Ti-containing steel than in the base steel as most RA was co-located between bainitic ferrite with parallel arrangement of laths in the former steel. Depending on the location of RA and the developed stress state, its stability in tension declines in the following order: RA in bainite > RA at polygonal ferrite/bainite interfaces > RA embedded in polygonal ferrite grains and at polygonal ferrite triple junctions or grain boundaries. Fine grains of RA may be less stable than their coarser counterparts if they are located in unfavorable stress regions of the microstructure.

## INTRODUCTION

The successful design of advanced high-strength steels relies on an in-depth understanding of the interrelationships among alloy composition, the end microstructure after thermo-mechanical processing (TMP) and desirable mechanical properties. In many steel grades, such as transformation-induced plasticity (TRIP)-assisted, quenched and partitioned (Q&P), and medium Mn TRIP steels, for example, the general aim was to achieve a desired fraction of retained austenite (RA) within the microstructure after various thermo-mechanical processing routes. This stemmed from research in the 1980s and onwards that showcased the importance of the deformation-induced transformation of RA to martensite in increasing the work hardening rate and improving the strength, ductility and crash resistance of alloys.<sup>1–5</sup> It follows that the extrema of RA rapidly transforming during the early stages of deformation or not transforming at all by the end of

it are not beneficial to improving the alloy's mechanical properties.<sup>6–9</sup> Consequently, and to maximize the positive effects bestowed by RA, the metastable phase needs to exhibit a gradual rate of transformation throughout deformation. Thus, efforts were directed at elucidating the factors controlling so-called RA stability (i.e., its resistance to martensite transformation under stress/strain), as addressed in several reviews.<sup>10,11</sup>

It is now well known that the chemical and mechanical stability of RA is influenced by several factors such as carbon and manganese concentrations in RA,<sup>5,12–16</sup> its size,<sup>7,15–18</sup> morphology<sup>6,8,13,19</sup> and orientation,<sup>20–23</sup> its location and neighboring phases<sup>4,6,22,24,25</sup> as well as the directionality of the imposed macroscopic stress.<sup>26–28</sup> Consequently, it is not a trivial task to determine whether a single or a combination of factors plays a dominant role in dictating RA stability. Furthermore, depending on the conditions, the same factors may exert opposite effects. This is because RA stability is also related to the complexity and variety of microstructures that form during TMP, particularly in multiphase TRIP steels, as well as differences in the stress/strain states

(Received April 28, 2021; accepted August 30, 2021;  
published online September 21, 2021)

of the individual constituents within the microstructure. Therefore, reports on the factors responsible for RA stability remain controversial to date.

The microstructure of low-carbon TRIP-assisted steels typically consists of ~40–60% equiaxed polygonal ferrite (PF), 30–40% carbide-free bainite with 5–20% of RA and martensite making up the remainder. Two types of carbide-free bainite are usually present:<sup>29</sup> (1) parallel laths of ferrite with interlayers of RA and martensite, which is termed bainitic ferrite (BF), or acicular ferrite (AF) when laths have multiple orientations, and (2) granular bainite (GB), which comprises irregular-shaped ferrite plates with RA and RA/martensite islands.

Although it was initially believed that higher carbon contents in RA would result in increased chemical stability, it was subsequently found not to always be the case. Depending on the processing, neighboring phases and size, the carbon distribution may not be uniform between<sup>30–33</sup> and within<sup>10,34</sup> RA grains, leading to its partial transformation to martensite in carbon-depleted regions. Furthermore, Refs. 14, 35, 36 showed that the presence of Mn, which is an austenite stabilizer like carbon, also influences RA stability. In this case, while up to 3.3 wt% Mn is beneficial, further increases in Mn up to 4.7 wt% affect the partitioning of carbon in RA thereby reducing the latter's chemical stability.<sup>14</sup> Alternatively, Tirumalasetty et al.<sup>35</sup> linked the reduction in RA stability in Mn-rich grains with additional internal stresses due to the inhomogeneous distribution of Mn. While film-like RA in bainite was generally considered to have a higher carbon content than those in PF,<sup>37</sup> subsequent atom probe tomography and electron energy loss spectroscopy investigations<sup>31</sup> showed that the carbon distribution of RA in different areas of bainite is also heterogeneous. It depends on the size of the prior austenite region from which the BF/GB formed, and in some instances, RA in PF has an even higher carbon content than those in BF.

With respect to mechanical stability, it is generally accepted that coarser-sized RA transforms earlier than finer ones.<sup>6,7,15,17</sup> This is related to the number of potential nucleation sites (slip steps and stacking faults) available. In addition, it is believed that smaller RA grains have higher carbon content; thus, their higher chemical stability aids their mechanical stability.<sup>17,20</sup> However, this was contested by Xiong et al.<sup>31</sup> who showed that some smaller RA grains possess lower carbon content than coarser ones. More recent research showed that large RA grains remain untransformed and may form either deformation twins or subgrains, both of which reduce the free path for dislocations and increase the resistance to martensite transformation.<sup>38</sup> The orientation of RA grains also exerts a significant effect.<sup>26</sup> For example, grains whose {200} planes are oriented at 0° and 90° to the tensile direction are more susceptible to martensite transformation.<sup>18,20</sup> Knijf et al.<sup>39</sup> reported that grains

oriented < 45° or perpendicular to the tensile direction transformed first because of the higher tensile and shear stresses on them. Furthermore, the rate of transformation to martensite is a function of the stress state, with the highest rates for plane strain tension, lowest rates for uniaxial compression, and intermediate rates for equi-biaxial and uniaxial tension.<sup>28</sup>

The effect of RA morphology on its stability is probably the most controversial factor. The reason for this is the isolated consideration of its morphology separate from the effect of neighboring phases, namely, their effect on solute partitioning into RA, response to plastic deformation and load transfer between neighboring phases.

Knijf et al.<sup>39</sup> suggested that large aspect ratio RA grains were less stable than globular RA without referencing its surrounding neighborhood. Contradicting this observation, some studies reported that film-like RA is more stable than RA surrounded by PF because of the former's high C content, higher hydrostatic pressure and stress shielding by BF laths<sup>37,40–42</sup>. Timokhina et al.<sup>6</sup> found that RA located between PF grains has the lowest stability, followed by RA located at the interfaces between PF and bainite and then by RA films in BF. Contrarily, Tomota et al.<sup>43</sup> suggested that due to the stress relaxation in PF, blocky RA enclosed by PF tends to be more stable. In further agreement, Tirumalasetty et al.<sup>21</sup> and Lomholt et al.<sup>44</sup> suggested that RA grains located at PF grain boundaries are the first to transform, whereas RA fully embedded within PF grains transforms later upon rotation.<sup>21</sup> On the other hand, Zhang and Findley<sup>45</sup> compared the stability of RA within BF and PF, respectively. Their analysis showed that the differences in stress partitioning between BF or PF and adjacent RA did not affect the latter's stability. Rather, the higher stability of RA within BF was linked to its higher chemical stability on account of the higher carbon content.

Based on the above, the complexities related to RA stability in TRIP steels and the dominance of individual or combinations of factors continues to be under debate. In this article, we utilize electron back-scattering diffraction (EBSD) to clarify the effects of RA morphology, its size and neighboring phases in thermo-mechanically processed low Si, high Al TRIP steels subjected to uniaxial tension. Although EBSD investigations on RA stability were previously reported, for example, Refs. 21, 23, 25, 39, 44, 46, most of them did not segment the bcc phases to evaluate the individual effects of PF and ferrite in bainite and martensite.

## EXPERIMENTAL PROCEDURE

Two 6-mm-thick hot-rolled plates were received from GIFT-POSTECH. Their compositions are given in Table I. Hereafter, a low Si, high Al steel and one with further Ti and Nb additions are referred to as the base and Nb–Ti steels,

**Table I. Nominal chemical composition of studied TRIP steels in wt%**

Steel	C	Mn	Si	Al	P	Nb	Ti
Base	0.15	2.00	0.30	1.00	0.05	–	–
Nb–Ti	0.15	2.00	0.30	1.00	0.01	0.03	0.02

respectively. Samples of 8 (rolling direction, RD)  $\times$  20 (transverse direction, TD)  $\times$  6 (normal direction, ND) mm<sup>3</sup> were electro-discharge machined and thermo-mechanically processed using a Gleeble 3500 simulator. The TMP schedule<sup>47</sup> involved heating at 2 °C s<sup>-1</sup> to an austenization temperature of 1250 °C followed by a 120 s hold and then cooling to 1100 °C where a 25% thickness reduction was applied via plane strain compression followed by a 120 s hold. Then, the samples were cooled to a finish rolling temperature of 850 °C for the base steel and 875 °C for the Nb–Ti steel where a further 47% thickness reduction was applied. This was followed by 1 °C s<sup>-1</sup> cooling to the accelerated cooling start temperature of 680 °C for the base steel and 690 °C for the Nb–Ti steel to form ~50% polygonal ferrite. To avoid pearlite formation, the cooling rate was increased to 20 °C s<sup>-1</sup> on cooling to the bainite formation temperature of 470 °C where the samples were held for 1200 s before water quenching to room temperature.

Dog-bone-shaped tensile test specimens with gauge dimensions 7 (length)  $\times$  3 (width)  $\times$  0.9 (thickness) mm<sup>3</sup> were produced by electro-discharge machining from the TMP samples. Uniaxial tension was conducted at a constant strain rate of  $4.5 \times 10^{-4}$  using an in-house modified 5kN Kammrath and Weiss GmbH mini-tensile stage. The yield strength (YS) was defined as the 0.2% offset proof stress. The work hardening rate ( $\Theta = d\sigma/d\varepsilon$ ) and the strain hardening exponent ( $n = (\varepsilon/\sigma)\Theta$ ) were calculated from the true stress versus true strain curves.

Following the tensile test, the samples were first sectioned along the tensile direction and then cut along the TD into three parts corresponding to: (1) the end undeformed grip section of the sample (nominally corresponding to 0 strain), (2) the quarter gauge length section of the sample which had undergone uniform elongation up to the ultimate tensile strength (UTS) and (3) the middle necked section of the sample containing the fracture. The RD-ND cross-sections of all three samples were electropolished using a Struers Lectropol-5 with an electrolyte containing 330 ml methanol, 330 ml butoxyethanol and 40 ml perchloric acid at 50 V, ~0.95–1.2 mA, 17 °C for 90 s.

EBSD maps were collected on a JEOL JSM-7001F field emission gun-scanning electron microscope operating at 15 kV and ~5 nA and fitted with a Nordlys-II detector interfacing with the AZtec software suite. A step size of 50 nm and map size 105  $\times$  79  $\mu\text{m}^2$  was maintained constant for all conditions.

The acquired maps were cleaned by removing wild orientation spikes. Unindexed areas tended to concentrate at grain boundaries and were filled in by extrapolating up to six neighbors. Throughout cleaning, the minimum misorientation for grain reconstruction was 2° and the grain boundary completion angle was 2°.

The raw EBSD maps comprised two phases, face-centered cubic (fcc) austenite and body-centered cubic (bcc) ferrite, and non-indexed areas. In this study, four phases, namely, polygonal ferrite (PF), ferrite in bainite, RA and martensite, were distinguished via a segmentation procedure using the grain orientation spread and grain size criteria.<sup>48</sup> The threshold values used for segmentation were based on an evaluation of the slope of the normalized cumulative distribution with respect to the origin.<sup>49</sup> The threshold value corresponded to the point when the change in the slope with respect to the origin tended to 1. The segmentation procedure is described in greater detail in Refs. 48–50. Low-angle boundaries are between  $2^\circ \leq \theta < 15^\circ$  whereas high-angle boundaries are between  $15^\circ < \theta < 62.8^\circ$ . A minimum spatial resolution of six times the nominal step size was maintained constant in all maps.

## RESULTS

The representative stress-strain, work hardening and instantaneous  $n$  curves for the base and Nb–Ti steels were previously reported in Ref. 47 and are shown in Fig. 1. The Nb–Ti steel depicts a slightly better combination of tensile properties (YS =  $476 \pm 7$  MPa, UTS =  $749 \pm 20$  MPa, uniform elongation (UE) =  $18 \pm 0\%$  and total elongation (TE) =  $29 \pm 0\%$ ) compared to the base steel (YS =  $445 \pm 44$  MPa, UTS =  $722 \pm 34$  MPa, UE =  $15 \pm 0\%$  and TE =  $25 \pm 4\%$ ). As stated in Ref. 47, the base steel exhibited continuous yielding and correspondingly smooth work hardening and instantaneous  $n$  curves. Contrarily, somewhat discontinuous yielding was noted for the Nb–Ti steel, with the work hardening and instantaneous  $n$  curves declining steeply up to ~0.01 strain and then reaching local maxima at ~0.02 and ~0.05–0.08 strain, respectively.

The segmented EBSD maps at 0 strain, UTS and fracture are shown in Fig. 2. The microstructure at 0 strain is characterized by bands of PF (~75% area fraction) and bainite (~18%) on account of the latter's transformation from pancaked prior austenite. The RA and martensite phases comprise the remainder of the microstructure. The overall microstructure was finer in the Nb–Ti steel than in the base steel with PF grain sizes of  $8 \pm 4 \mu\text{m}$  versus  $12 \pm 6 \mu\text{m}$ , respectively. Most of the RA was confined to bainite with only a small amount present in PF. Two morphologies of bainite are clearly seen in the EBSD maps: (1) granular bainite with high internal misorientation neighboring small fractions of blocky RA or RA/martensite constituent

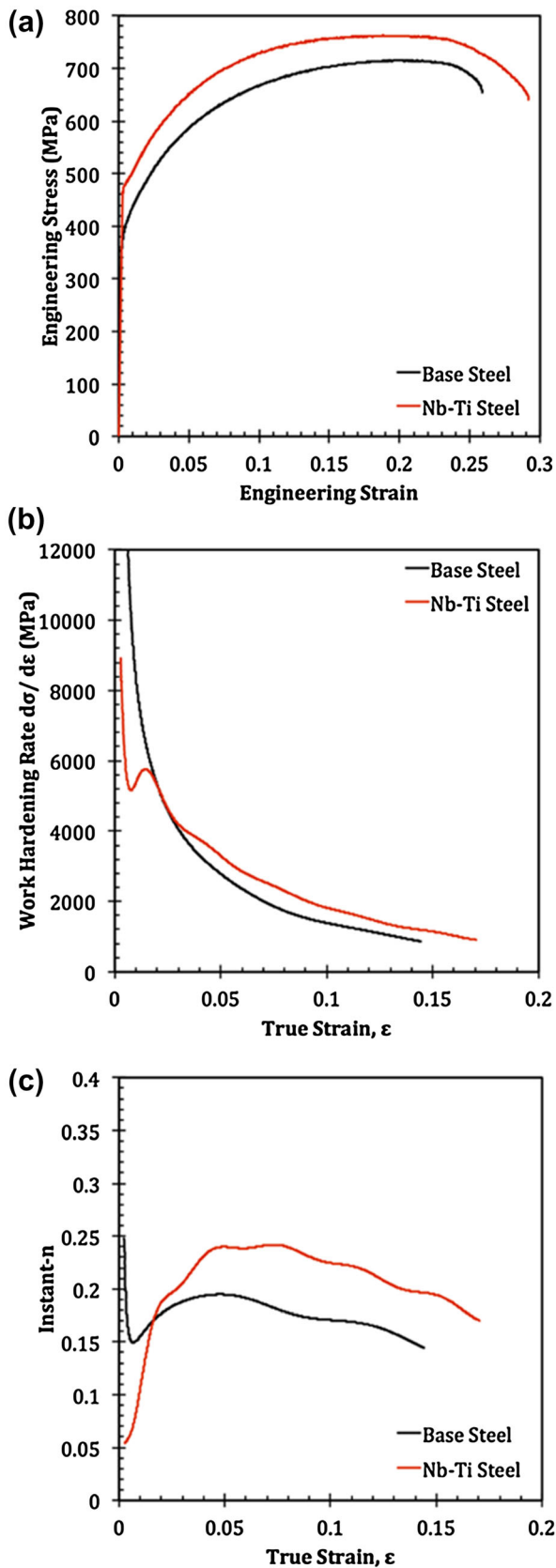


Fig. 1. (a) The engineering stress-strain curves, (b) work-hardening rate and (c) instantaneous  $n$ -value as a function of true strain.

and (2) bainitic ferrite interlayered with relatively coarse RA ( $\sim 0.2\text{--}1\ \mu\text{m}$  thick). The initial area fraction of martensite was due to the transformation of a small fraction of low stability RA (probably due to its relatively low carbon content) during quenching from isothermal holding.

Localized areas of high strain at fracture resulted in the white unindexed areas in Fig. 2e and f. The unindexed areas are predominantly located near grain boundaries and at interfaces between phases/ferrite morphologies. Based on the nominally indexed values, the rate of decrease in RA and increase in martensite area fractions from 0 strain to UTS and fracture is higher in the Nb-Ti steel compared to the base steel (Table II). However, the area fractions of PF and bainite in these maps vary on account of the three strains being represented by three different samples. It follows that the rates of decrease and increase in RA and martensite area fractions could be misrepresentative of the actual trend. To account for this, the area fractions of RA and martensite at different strains were normalized with respect to the sum of polygonal ferrite and bainite fractions (i.e., the non-transforming phases). As seen in Table II, the normalized values of RA and martensite are similar to their nominally indexed counterparts\*.

Figure 3a and b shows the distributions of equivalent grain diameter of RA for both steels at different strains; with the  $0.15\ \mu\text{m}$  minimum grain size being six times the EBSD map step size. The average RA grain size at 0 strain is slightly coarser in the base steel compared to the Nb-Ti steel. At fracture, the remaining RA had grain sizes  $< 1\ \mu\text{m}$  in the base steel and  $< 0.7\ \mu\text{m}$  in Ni-Ti steel.

The relative frequencies of the  $3 \times 3$  kernel average misorientation (KAM) at different strains are shown in Fig. 4a and c for the bcc phases/morphologies (PF, ferrite in bainite and martensite) and the fcc phase (RA). With higher tensile strain, the peaks shift rightwards to higher mean KAM values along with an overall broadening of the distribution. This indicates an increase in the accumulated strain in the phases.

The variation in the mean local misorientation at different strains is presented in Fig. 4b and d. In both steels, the small standard deviation values for PF at 0 strain are due to the low orientation gradient within PF grains. For PF, the mean KAM increased by  $\sim 150\%$  between 0 strain and fracture in the base steel whereas the increase was  $\sim 183\%$  in the Nb-Ti steel. For ferrite in bainite, the mean KAM increased by  $\sim 10\%$  between 0 strain and fracture in the base steel and  $\sim 85\%$  in the Nb-Ti

\*In theory, the normalized area fraction of martensite at fracture should be approximately equal to the sum of the normalized area fractions of RA and martensite at 0 strain. However, the above logic holds true only when the same area is tracked at different strains. It is reemphasised that this is not the case in the present study.

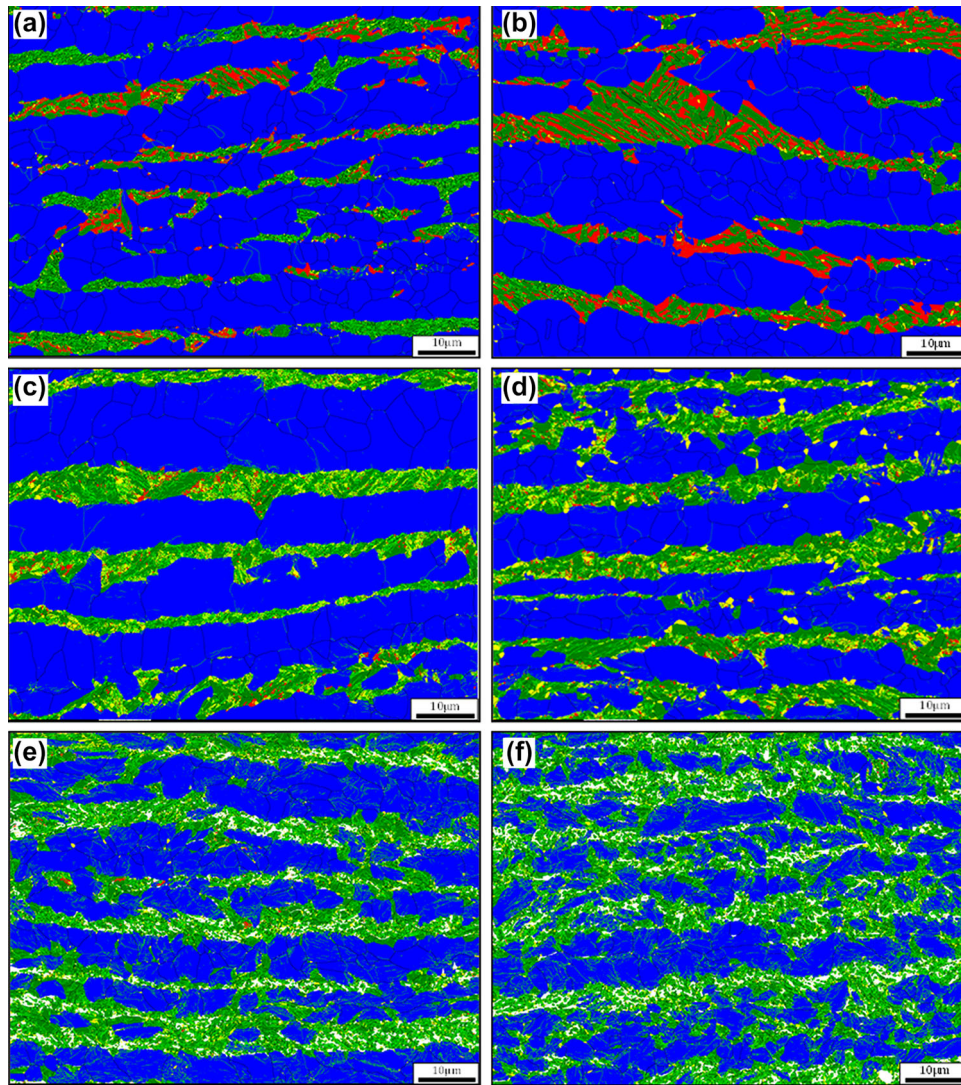


Fig. 2. EBSD phase maps for the base steel (a, c and e), and Nb–Ti steel (b, d and f) at three different tensile deformation conditions; after TMP (zero tensile strain, a and b), at UTS (c and d) and at fracture (e and f). HAGBs = black color; LAGBs = light green color. The polygonal ferrite (PF) = blue, retained austenite (RA) = red, ferrite in bainite = green and martensite = yellow; white are non-indexed areas. RD = map horizontal; ND = map vertical. (a and b) are adopted from Ref. 50 with permission from Elsevier, Copyright 2014 (Color figure online).

steel. For RA, the mean KAM increased by  $\sim 30\%$  between 0 strain and fracture in the base steel whereas the increase in the mean KAM value in the Nb–Ti steel was  $\sim 100\%$ .

As mentioned previously, RA formed various morphologies due to the TMP applied in this study and was found in different locations in the EBSD maps of the two steels. As a result, an aspect ratio of 1.5 was used to differentiate film and blocky-type RA morphologies. The results showed that an  $\sim 0.65\text{--}0.73$  area fraction of RA had a film-like morphology whereas an  $\sim 0.27\text{--}0.35$  area fraction comprised blocky-type morphology in both steels. Table III shows the exact amount of RA in each phase and the RA morphology in bainite as a function of strain. For this analysis, any RA located at PF/bainite interfaces at 0 strain was allocated to bainite. To confirm the effect of RA grain shape on

its stability while mitigating subgrain size effects, morphological analysis was also applied on large RA grains. Nevertheless, the ratio of the blocky-type to the film-like RA remained the same as in Table III.

Select examples of RA grain response when located in different areas are shown in Figs. 5 and 6. Small RA grains located at PF interfaces transform fully to martensite (Fig. 5a). While coarse RA grains embedded within PF grains undergo partial transformation (Fig. 5b), small RA grains within the PF do not transform (Fig. 5c). As shown in Fig. 5, the fraction of low-angle boundaries in the immediate vicinity of untransformed RA and transformed martensite grains is higher than in other parts of the matrix. These areas evidence local strain fields such that the increase in geometrically necessary dislocation (GND) density is concurrent with their rearrangement into low energy configurations. The local

**Table II. Summary of the unindexed and phase area fractions in the base steel and Nb-Ti steel at different strains**

Steel	Strain	unIdx	PF	Bainite	RA		Martensite	
					Nominal	Normalized	Nominal	Normalized
Base	$\varepsilon = 0$	0	0.776	0.165	0.05	0.053	0.009	0.010
	UTS	0	0.743	0.177	0.012	0.013	0.068	0.074
	$\varepsilon = 15\%$							
	Fracture	0.043	0.650	0.260	0.0027	0.003	0.046	0.051
Nb-Ti	$\varepsilon = 25\%$							
	$\varepsilon = 0$	0	0.713	0.188	0.094	0.104	0.005	0.006
	UTS	0	0.643	0.255	0.014	0.016	0.088	0.098
	$\varepsilon = 18\%$							
	Fracture	0.060	0.600	0.280	0.0006	0.001	0.06	0.068
	$\varepsilon = 29\%$							

*unIdx* unindexed, *PF* polygonal ferrite, *RA* retained austenite

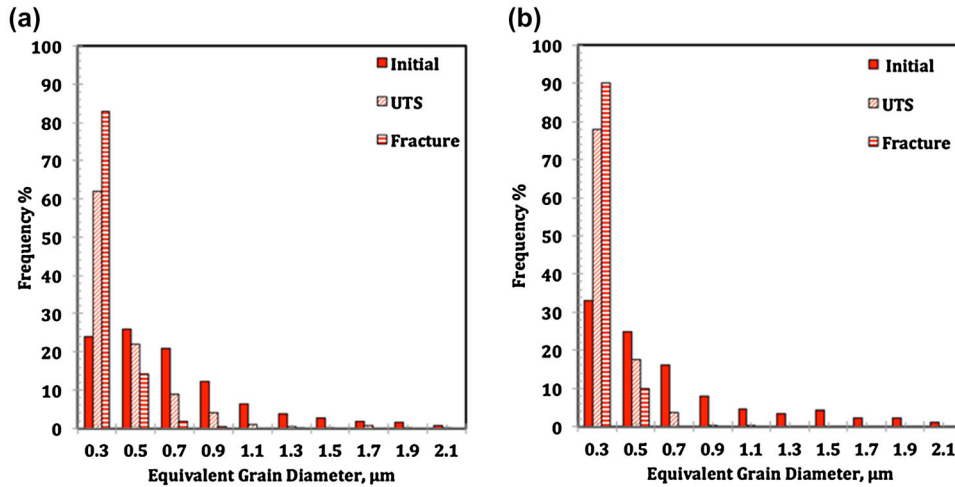


Fig. 3. (a, b) The equivalent subgrain diameter of retained austenite variation during tensile test for (a) base steel and (b) Nb-Ti steel (Color figure online).

increase in GNDs was required to accommodate: (1) the inhomogeneity of plastic deformation around hard RA/martensite crystals in PF and (2) the volume expansion accompanying martensitic transformation. In both steels, there is a considerable amount of RA at the interface of bainite and PF, a significantly larger fraction of which transformed to martensite after tension compared to RA located within the bainite. The former observation is also apparent when noting the higher numbers of martensite grains at martensite-bainite/PF interphases at UTS (Fig. 5d and e). The orientation and shape of RA grains with respect to PF/bainite interfaces also affect their stability. The remaining RA grains located at the PF/bainite interfaces tend to (1) be parallel to the interface (Fig. 5d-e) or (2) protrude in PF grains (Fig. 5d and f). It is observed that the stability of protruding RA grains is higher than for

RA grains that are oriented parallel to PF/bainite interfaces as most of the RA grains oriented parallel to the PF/bainite interface tend to transform to martensite at UTS. It is also worth highlighting that, in many instances, coarse blocky and lath-like RA only partially transforms to martensite (Fig. 6). This subdivision leads to (1) an increase in small-sized RA grains and (2) a change in aspect ratio from long film-like morphologies to smaller blocky RA instead.

At fracture, the area fraction of RA grains remaining at PF/bainite interfaces and embedded within bainite/martensite clusters was estimated to be  $\sim 0.3$  and  $\sim 0.7$  in the base and Nb-Ti steels, respectively. Most of these RA grains in both steels were located within the bainite with only very small numbers in base steel found at the PF/bainite interfaces.

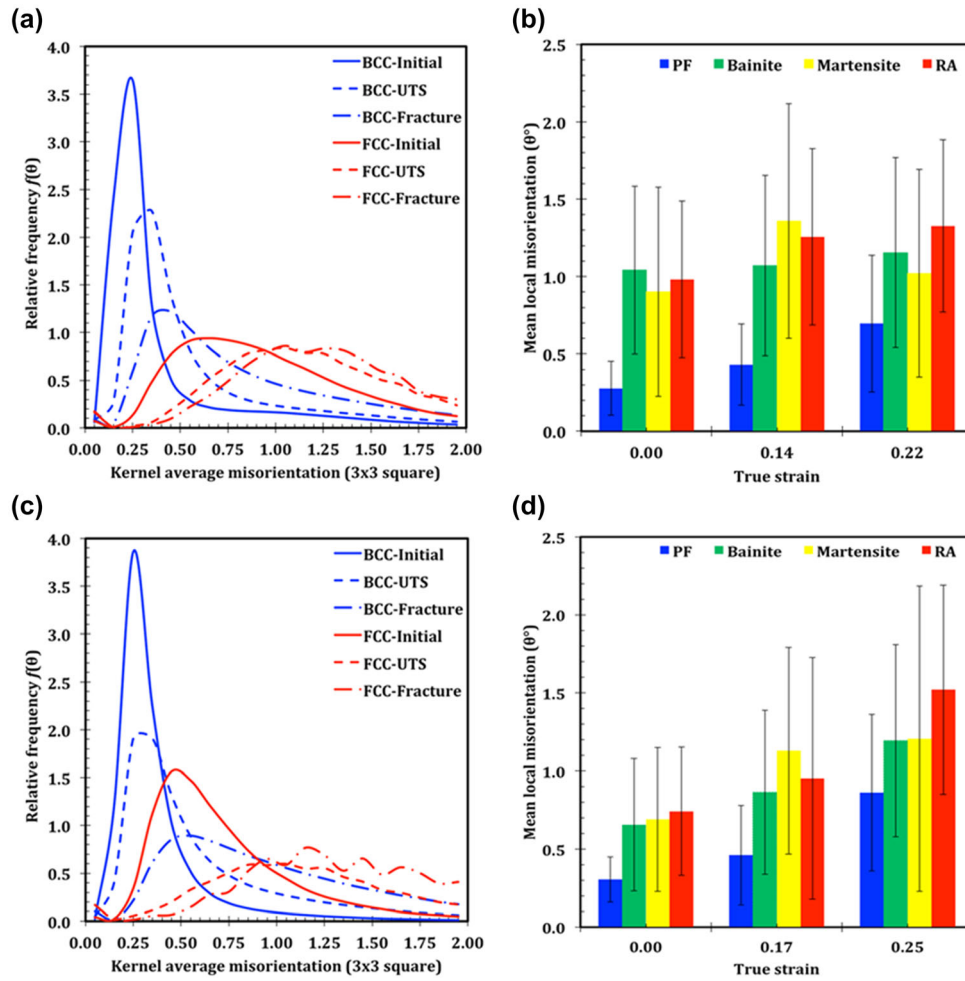


Fig. 4. Kernel average misorientation distribution of the bcc [bainite, polygonal ferrite (PF) and martensite] and retained austenite (RA) phases at different tensile strains (a and c) and the mean and standard deviation of the KAM value for each phase/morphology (b and d) for base (a and b) and Nb-Ti (c and d) steels (Color figure online).

**Table III. Effect of tension on the area fractions of various retained austenite (RA) morphologies located in polygonal ferrite (PF) and bainite**

Steel	Strain	RA in PF	RA in bainite		Total
			Blocky (AR ≤ 1.5)	Film (AR > 1.5)	
Base	$\epsilon = 0$	0.013	0.270	0.730	0.987
	UTS	~0	0.332	0.668	~1
	$\epsilon = 15\%$				
Nb-Ti	Fracture	~0	0.338	0.662	~1
	$\epsilon = 25\%$				
	$\epsilon = 0$	0.005	0.345	0.655	0.995
Nb-Ti	UTS	~0	0.347	0.653	~1
	$\epsilon = 18\%$				
	Fracture	~0	0.344	0.656	~1
Nb-Ti	$\epsilon = 29\%$				

AR grain aspect ratio

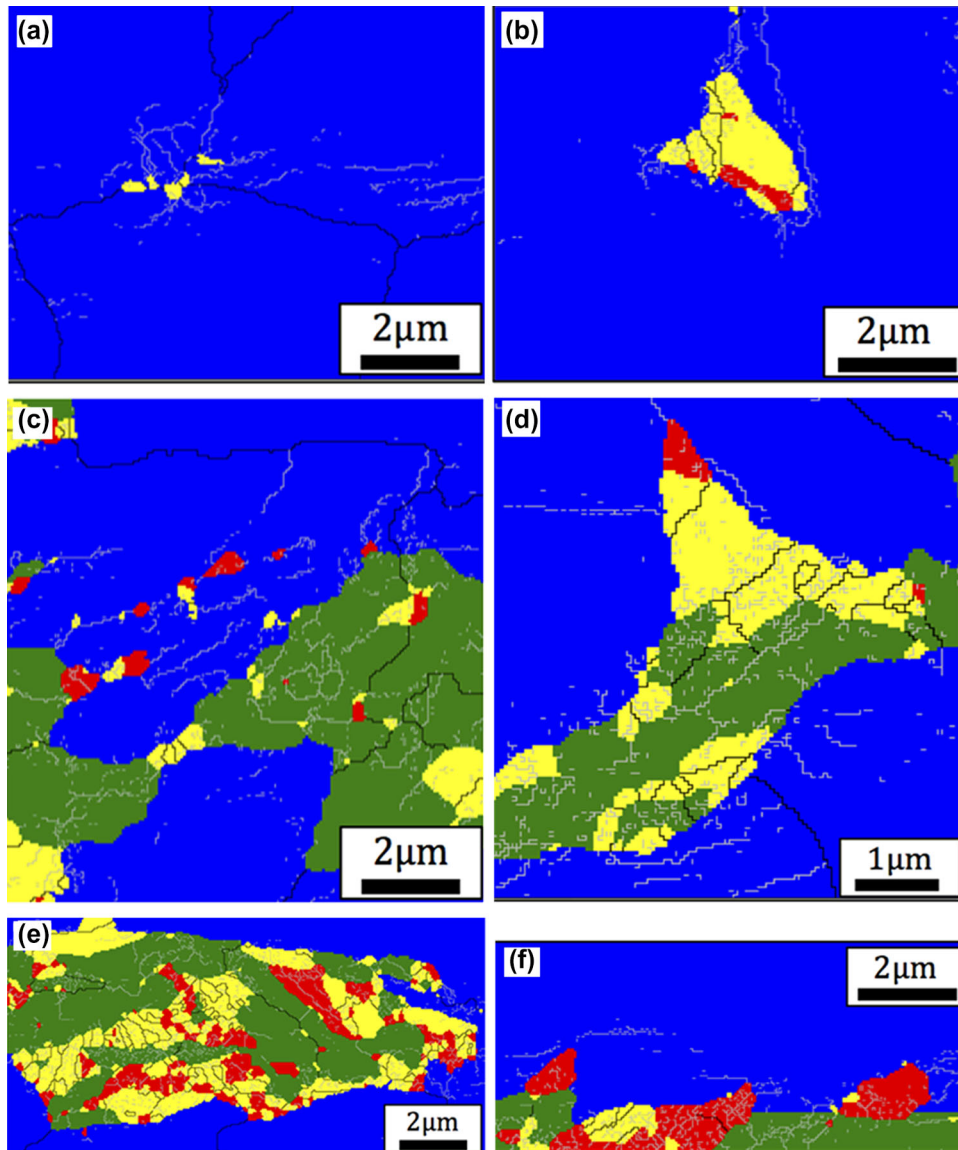


Fig. 5. EBSD phase maps showing examples of retained austenite state after deformation: retained austenite in polygonal ferrite (a–c); retained austenite at polygonal ferrite/bainite interfaces (d–f). (a, b, f and d) Base steel; (c, e) Nb–Ti steel. HAGBs = black color; LAGBs = light green color. The polygonal ferrite (PF) = blue, retained austenite (RA) = red, ferrite in bainite = green and martensite = yellow; white are non-indexed areas. RD = map horizontal; ND = map vertical (Color figure online).

## DISCUSSION

### Effect of Strain on the Internal Misorientation of Different Phases/Morphologies

The maps at fracture contain unindexed areas. Therefore, the KAM calculations for all phases/morphologies may suffer from some error related to the non-inclusion of the unindexed areas. Generally speaking, the highest KAM values were predominantly returned at/near the grain boundaries due to the accumulation of dislocation tangles at the grain boundary.<sup>51</sup> The effect of volume expansion when RA transforms to martensite on the local misorientation gradient in ferrite was also observed in DP steels containing 24%–38% martensite.<sup>52</sup>

It was previously reported that strain partitioning varies according to the microstructure and chemical composition.<sup>53</sup> However, Fig. 4 showed that PF had low mean KAM values compared to harder phases such as bainite and martensite. Accordingly, the plastic strain during tension will not be uniformly distributed in this multi-phase steel. PF will tend to yield first, and, following a period of work hardening, the stress is then transferred to harder phases such as austenite, bainite and martensite.<sup>54,55</sup> In agreement with the above, and in both steels, the mean KAM values at 0 strain were the lowest for PF and the increase in mean KAM values from 0 strain to fracture was the highest in PF compared to other phases/ferrite



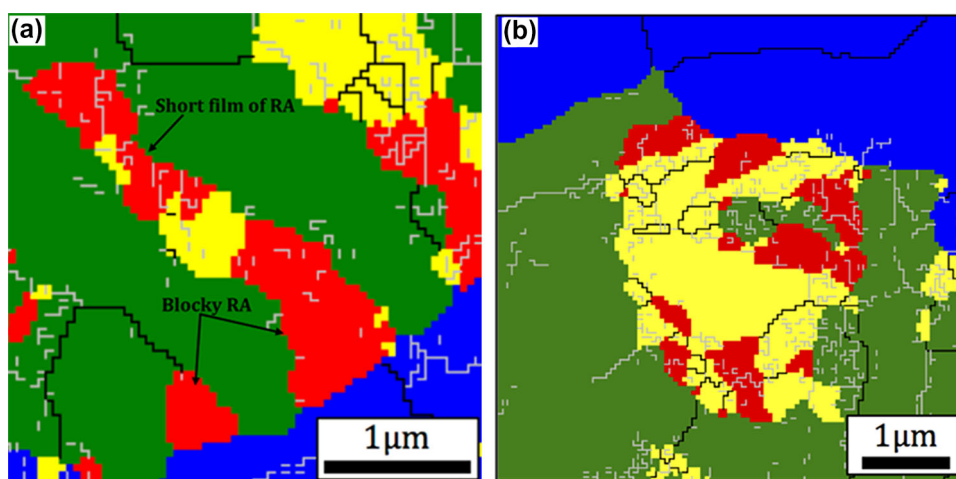


Fig. 6. The partial transformation of the film (a) and blocky (b) retained austenite grain in bainite in the Nb–Ti steel at UTS. HAGBs = black color; LAGBs = light green color. The polygonal ferrite (PF) = blue, retained austenite (RA) = red, ferrite in bainite = green and martensite = yellow. RD = map horizontal; ND = map vertical (Color figure online).

morphologies (Fig. 4c and 4d) and is associated with the rapid work hardening of PF.

In both steels, the mean KAM values of RA at 0 strain were relatively higher than PF due to the deformation applied in the non-recrystallization region during TMP. Between UTS and fracture, RA tended to higher mean KAM values at quicker rates compared to bainite and martensite.<sup>56</sup> The above is contrary to previous work on the uniaxial tension of Q&P steel, which showed that the rate of increase in KAM values in RA surrounded by martensite was much slower than that of martensite and that strain concentrations were localized at RA/martensite interfaces.<sup>25</sup>

Compared to the base steel, the quicker rates to higher mean KAM values in RA in the Nb–Ti steel were also associated with the quicker rates to higher mean KAM values in ferrite in bainite. This finding is predictable since most of the RA is located within bainite in both steels. KAM analysis in Ref. 46 on a TRIP steel showed that when the mean KAM value increased by 10% in RA, the mean KAM of ferrite (which in that study included PF, ferrite in bainite and martensite) increased by almost 100%. The latter can be explained by the overall higher strain accommodated by bcc phases/morphologies, which comprised the majority phase fraction compared to the minor fcc phase fraction. However, that study did not distinguish between various bcc phases/morphologies.

In contrast, the mean KAM value of  $1.04^\circ$  for ferrite in bainite in the base steel is significantly higher than the  $0.66^\circ$  calculated for the Nb–Ti steel. Between 0 strain and fracture, the mean KAM for ferrite in bainite increased by  $\sim 10\%$  in the base steel and  $\sim 85\%$  in the Nb–Ti steel. Differences in the predominant bainite phase morphology in the base and Nb–Ti steels help explain the large

variation in KAM values at 0 strain as well as the increase in mean KAM values from 0 strain to fracture. The predominant GB morphology in the base steel as opposed to BF in the Nb–Ti steel is suggested as the reason for the difference in mean KAM values at 0 strain.<sup>47,50</sup>

### On the Stability of Retained Austenite

In agreement with multiple reports,<sup>1,6,18,19,24,57</sup> this study also shows a significant reduction in the volume fraction of RA with uniaxial tension. The decrease in the normalized area fraction of RA was more drastic in Nb–Ti steel (from  $\sim 0.104$  to  $\sim 0.001$ ) than the base steel (from  $\sim 0.053$  to  $0.003$ ). In the following paragraphs, the stability of RA is discussed with respect to its location in three different regions: (1) within PF, (2) at PF/bainite interfaces and (3) within bainite.

As seen in Table III, the area fraction of RA within PF at 0 strain is far lower than in bainite. Between 0 strain and UTS, nearly all RA in PF either fully or partially transformed to martensite. Similar results were reported in Ref. 6 where only the 0.02 and 0.05 area fraction of RA remained from starting fractions of 0.13 and 0.11 between PF grains in the base and Nb high Si TRIP steels, respectively. In that study, all RA grains transformed to martensite after 0.1 strain. In general, the low stability of RA within PF is related to the latter being the softest among all phases and its rapid work hardening at the start of deformation. Following a period of PF work hardening, and since the yield strength of RA is higher than that of PF<sup>43</sup> due to its higher carbon content, the load transfers over to the RA within PF grains.

The stability of RA within PF depends on the exact RA location, for instance, at PF triple

junctions, between PF grain boundaries or within the interior of PF grains. Similar to the observations made by Tirumasetty et al.<sup>21</sup> and Lomholt et al.<sup>44</sup>, the RA located at PF triple junctions (Fig. 5a) fully transformed to martensite whereas the RA embedded within PF grains, depending on their size, either remained untransformed or was partially transformed (Fig. 5b and 5c). Due to the inhomogeneity of plastic deformation, the transformation of RA located at boundaries/triple junctions is facilitated on account of differently oriented neighboring PF grains at its interfaces, the development of higher stresses at grain boundaries and their junctions and a triaxial stress condition in RA grains. In the case of RA embedded within PF grains, GNDs form around them to accommodate the inhomogeneity of plastic deformation. The load transfer to RA takes place after sufficient work hardening of the surrounding PF. These RA grains then rotate to accommodate the deformation before their subsequent transformation to martensite<sup>21</sup> or remain untransformed. The observed RA behavior agrees with Ref. 26 where ferrite grain boundaries and the number of surrounding PF grains influenced the stability of RA within PF. However, there is also a size effect on RA stability, which may be related to the non-uniform distribution of carbon and Mn within RA. It is speculated that small RA grains are more uniformly enriched in carbon, and possibly Mn, such that they remain untransformed. On the other hand, the carbon and Mn distribution in coarser RA grains tends to be more non-uniform (Fig. 5b) such that they subsequently undergo partial transformation.

The RA grains located at PF/bainite interfaces showed an intermediate resistance to transformation with many relatively large RA grains protruding into PF remaining untransformed at UTS (Fig. 5f). In Refs. 7, 24, 30–33, 58, it was reported that the non-uniform distribution of carbon between and within different RA grains, and the partial transformation of parts of RA grains, could be responsible for an overall reduction in the stability of RA. Consequently, the partial transformation observed in parts of RA grains close to PF in this study (Fig. 5e) could be explained by the influence of the low chemical stability of RA as well as the higher stresses at/near interface regions. The chemical inhomogeneity in RA at PF/bainite interface arises from carbon partitioning to RA during the formation of bainite. If the diffusivity of carbon is assumed to be  $1.71 \times 10^{-16} \text{ m}^2/\text{s}$ , estimations of the diffusion distance for carbon at 470 °C in 1200 s (i.e., the simulated coiling stage during TMP) returned to 0.5  $\mu\text{m}$ . Thus, carbon could not reach the center of RA grains > 1  $\mu\text{m}$  in size. However, some RA grains > 1  $\mu\text{m}$  remain untransformed. These protruding RA grains are embedded in one PF grain on two sides and are in contact with bainite on the other sides. Moreover, these RA grains show a higher density of low-angle boundaries as shown in Fig. 5f.

The subdivision of large RA grains into subgrains can be suggested as a factor that enhances the stability of RA because it reduces the effective volume for martensite nucleation. In the current study, the number of RA grains that experience enhanced stability by grain subdivision was not enough to statistically draw a definitive conclusion, but it remains a factor that may need further investigation.

Many RA grains at PF/bainite interfaces and within bainite partially transform to martensite (Figs. 5d-e and 6). This partial transformation led to three changes in the microstructure: (1) an increase in the area fraction of fine RA grains compared to the 0 strain condition, (2) a reduction in the aspect ratio of RA grains and (3) an increase in the area fraction of freshly formed martensite. The former is responsible for the standard general conclusion that finer RA grain sizes are the primary determinant of RA stability. However, from our earlier discussion, the location of fine-grained RA is a more crucial factor than size alone as the stress state dictates whether fine-grained RA remains stable or undergoes transformation (c.f. Fig. 5a and 5c). Partial transformation leads to the subdivision of RA into smaller volumes, and these small volumes may reach a critical size below which martensite transformation is not initiated. Furthermore, when RA is surrounded by a harder phase like ferrite in bainite or martensite, hydrostatic pressure is exerted on RA, which translates to a decrease in the martensite-start transformation temperature.<sup>59</sup> If RA is in contact with a hard phase which does not accommodate the stress, then that stress could be directly transferred to RA and trigger martensite formation.<sup>60</sup> However, if ferrite in bainite or fresh martensite has the capacity to strain harden, then it provides a shielding effect for RA, thereby increasing its mechanical stability.<sup>40</sup> This is the reason why thin films of RA and fine blocky RA resulting from the original subdivision of RA transform to martensite at later stages of tension or remain untransformed. The rate of transformation of RA within BF in the Nb–Ti steel was faster than the RA within GB in the base steel. This could be related to the faster rate of strain accumulation in the parallel arrangements of laths in BF compared to ferrite in GB of base steel (please refer to Sect. “Effect of Strain on the Internal Misorientation of Different Phases/Morphologies” re KAM). Thus, higher stresses accumulated at RA/BF lath boundaries assisted the transformation to martensite.

Both chemical and mechanical stabilities play a role in the deformation-induced transformation of RA to martensite. While the above discussion on the mechanical stability of RA (size and shape) is based on the analysis of two-dimensional EBSD maps, supplementary three-dimensional investigations, which account for RA grain shape and/or its surrounding neighborhood, are required. It is also clear that alloying elements, the phases present (which in

turn are affected by TMP history), phase characteristics (including size, morphology and defect substructure), the interaction between phases during deformation as well as the overall stress state play important and interrelated roles in RA stability and warrant further investigations.

### CONCLUSION

RA stability in two TRIP-assisted steels subjected to uniaxial tension was investigated using EBSD. Segmentation of the bcc phases into PF, ferrite in bainite and martensite during map post-processing enabled a better understanding of how deformation is accommodated in the studied steels and led to the following conclusions:

1. The rate of transformation of RA in the Nb–Ti steel was higher than in the base steel and is an indication of the higher stability of RA in the latter steel.
2. Phase segmentation enabled kernel average misorientation analysis of all phases/morphologies in both steels. The rate of increase in the mean KAM values of ferrite in bainite in the Nb–Ti steel was higher than in the base steel. This behavior was related to the predominant bainitic ferrite morphology in the Nb–Ti steel. Compared to granular bainite, the parallel lath arrangement of bainitic ferrite was deemed responsible for the lower stability of RA.
3. The partial transformation of RA grains could lead to misleading conclusions on the high stability of small RA grains. This study demonstrates that the partial transformation of large RA grains introduced smaller RA grains. Finer RA grains could be unstable depending on the stress state, for example, if located at PF triple junctions or between PF grain boundaries.
4. The locations of RA and neighboring stress states have a pronounced effect on RA stability in combination with its chemical stability (i.e., the amount and uniformity of enrichment by solutes). As a function of its location, RA stability was found to increase in the following order: PF grain boundaries/triple junctions < the interior of PF grains < PF/bainite interfaces < within bainite.

### ACKNOWLEDGEMENTS

The authors are grateful to POSCO and Profs. H. Kim and B.C. De Cooman, GIFT-POSTECH, for providing the steels. The EBSD work was undertaken on a JEOL JSM-7001F FEG-SEM funded by the Australian Research Council-Linkage, Infrastructure, Equipment and Facilities Grant LE0882613. The Oxford Instruments 80 mm<sup>2</sup> X-Max EDS detector was funded via the 2012 UOW Major Equipment Grant scheme.

### CONFLICT OF INTEREST

On behalf of all authors, the corresponding author states that there is no conflict of interest.

### SUPPLEMENTARY INFORMATION

The online version contains supplementary material available at <https://doi.org/10.1007/s11837-021-04880-y>.

### REFERENCES

1. O. Matsumura, Y. Sakuma, and H. Takechi, *Scr. Metall.* 21, 1301 (1987).
2. Y. Sakuma, D.K. Matlock, and G. Krauss, *J. Heat Treat.* 8, 109 (1990).
3. B.C. De Cooman, *Curr. Opin. Solid State Mater. Sci.* 8, 285 (2004).
4. P.J. Jacques, F. Delannay, and J. Ladrière, *Metall. Mater. Trans. A* 32A, 2759 (2001).
5. M.D. Meyer, D. Vanderschueren, and B.C.D. Cooman, *ISIJ Int.* 39, 813 (1999).
6. I.B. Timokhina, P.D. Hodgson, and E.V. Pereloma, *Metall. Mater. Trans. A* 35A, 2331 (2004).
7. E. Jimenez-Melero, N.H. van Dijk, L. Zhao, J. Sietsma, S.E. Offerman, J.P. Wright, and S. van der Zwaag, *Scr. Mater.* 56, 421 (2007).
8. X.C. Xiong, B. Chen, M.X. Huang, J.F. Wang, and L. Wang, *Scr. Mater.* 68, 321 (2013).
9. A. Itami, M. Takahashi, and K. Ushioda, *ISIJ Int.* 35, 1121 (1995).
10. E. Pereloma, A. Gazder, I. Timokhina, Encyclopedia of Iron, Steel, and Their Alloys, ed. R. Colas and G.E. Totten (New York: CRC Press, 2015) p. 3088.
11. B. He, *Materials* 13, 3440 (2020).
12. I. Timokhina, H. Beladi, X.-Y. Xiong, Y. Adachi, and P. Hodgson, *Acta Mater.* 59, 5511 (2011).
13. Y.F. Shen, L.N. Qiu, X. Sun, L. Zuo, P.K. Liaw, and D. Raabe, *Mater. Sci. Eng. A* 636, 551 (2015).
14. A. Grajcar, A. Kilarski, and A. Kozłowska, *Metals* 8, 929 (2018).
15. S. Lee, S.-J. Lee, and B.C. De Cooman, *Scr. Mater.* 66, 832 (2012).
16. Z.H. Cai, H. Ding, R.D.K. Misra, and Z.Y. Ying, *Acta Mater.* 84, 229 (2015).
17. A. Kammouni, W. Saikaly, M. Dumont, C. Marteau, X. Bano, and A. Charai, *Mater. Sci. Eng. A* 518, 89 (2009).
18. R. Blondé, E. Jimenez-Melero, L. Zhao, J.P. Wright, E. Brück, S. van der Zwaag, and N.H. van Dijk, *Acta Mater.* 60, 565 (2012).
19. F.G. Caballero, C. García-Mateo, J. Chao, M.J. Santofimia, C. Capdevila, and C.G. De Andres, *ISIJ Int.* 48, 1256 (2008).
20. S. Kruijver, L. Zhao, J. Sietsma, S. Offerman, N. van Dijk, E. Lauridsen, L. Margulies, S. Grigull, H. Poulsen, S. van der Zwaag, *J. de Phys. IV, EDP Sciences*, 499 (2003).
21. G.K. Tirumalasetty, M.A. van Huis, C. Kwakernaak, J. Sietsma, W.G. Sloof, and H.W. Zandbergen, *Acta Mater.* 60, 1311 (2012).
22. W.S. Li, H.Y. Gao, H. Nakashima, S. Hata, and W.H. Tian, *Mater. Sci. Eng. A* 649, 417 (2016).
23. D. De Knijf, T. Nguyen-Minh, R.H. Petrov, L.A.I. Kestens, and J.J. Jonas, *J. Appl. Cryst.* 47, 1261 (2014).
24. E.V. Pereloma, A.A. Gazder, I.B. Timokhina, *Mater. Sci. Forum*, 212 (2013).
25. W.-S. Li, H.-Y. Gao, H. Nakashima, S. Hata, and W.-H. Tian, *Mater. Charact.* 118, 431 (2016).

26. G. Reisner, E. Werner, P. Kerschbaummayr, I. Papst, and F. Fischer, *JOM* 49, 62 (1997).
27. P.J. Jacques, Q. Furnémont, F. Lani, T. Pardoën, and F. Delannay, *Acta Mater.* 55, 3681 (2007).
28. H. Kim, J. Lee, F. Barlat, D. Kim, and M.-G. Lee, *Acta Mater.* 97, 435 (2015).
29. S. Zajac, J. Komenda, P. Morris, P. Dierickx, S. Matera, F. Penalba Diaz, *Technical Steel Research Report*, EUR 21245EN. European Commission, Luxembourg, (2005).
30. C.P. Scott, and J. Drillet, *Scr. Mater.* 56, 489 (2007).
31. Z. Xiong, A. Saleh, R. Marceau, A. Taylor, N. Stanford, A. Kostryzhev, and E. Pereloma, *Acta Mater.* 134, 1 (2017).
32. N.H. van Dijk, A.M. Butt, L. Zhao, J. Sietsma, S.E. Offerman, J.P. Wright, and S. van der Zwaag, *Acta Mater.* 53, 5439 (2005).
33. E. Pereloma, I.B. Timokhina, M.K. Miller, and P.D. Hodgson, *Acta Mater.* 55, 2587 (2007).
34. I.B. Timokhina, E.V. Pereloma, S.P. Ringer, R.K. Zheng, and P.D. Hodgson, *ISIJ Int.* 50, 574 (2010).
35. G. Tirumalasetty, M. Van Huis, C. Kwakernaak, J. Sietsma, W. Sloof, and H. Zandbergen, *Scr. Mater.* 71, 29 (2014).
36. S. Lee, S.-J. Lee, and B.C. De Cooman, *Scr. Mater.* 65, 225 (2011).
37. Z. Xiong, G. Casillas, A.A. Saleh, S. Cui, and E.V. Pereloma, *Sci. Rep.* 7, 17397 (2017).
38. D. De Knijf, C. Föjer, L.A.I. Kestens, and R. Petrov, *Mater. Sci. Eng. A* 638, 219 (2015).
39. K. Sugimoto, M. Misu, M. Kobayashi, and H. Shirasawa, *ISIJ Int.* 33, 775 (1993).
40. J. Chiang, J.D. Boyd, and A.K. Pilkey, *Mater. Sci. Eng. A* 638, 132 (2015).
41. H.S. Park, J.C. Han, N.S. Lim, J.-B. Seol, and C.G. Park, *Mater. Sci. Eng. A* 627, 262 (2015).
42. K.K. Park, S.T. Oh, S.M. Baeck, D.I. Kim, J.H. Han, H.N. Han, S.-H. Park, C.G. Lee, S.-J. Kim, and K.H. Oh, *Mater. Sci. Forum* 408–412, 571 (2002).
43. Y. Tomota, H. Tokuda, Y. Adachi, M. Wakita, N. Minakawa, A. Moriai, and Y. Morii, *Acta Mater.* 52, 5737 (2004).
44. T.N. Lomholt, Y. Adachi, A. Bastos, K. Pantleon, and M.A. Somers, *Mater. Sci. Techn.* 29, 1383 (2013).
45. S. Zhang, and K. Findley, *Acta Mater.* 61, 1895 (2013).
46. R. Petrov, L. Kestens, A. Wasilkowska, and Y. Houbaert, *Mater. Sci. Eng. A* 447, 285 (2007).
47. F. Alharbi, A.A. Gazder, A. Kostryzhev, B.C. De Cooman, and E.V. Pereloma, *J. Mater. Sci.* 49, 2960 (2014).
48. A.A. Gazder, F. Al-Harbi, H.T. Spanke, D.R.G. Mitchell, and E.V. Pereloma, *Ultramicroscopy* 147, 114 (2014).
49. A.A. Gazder, M. Sanchez-Araiza, J.J. Jonas, and E.V. Pereloma, *Acta Mater.* 59, 4847 (2011).
50. E.V. Pereloma, F. Al-Harbi, and A.A. Gazder, *J. Alloys Compd.* 615, 96 (2014).
51. M. Kamaya, *Mater. Charact.* 60, 125 (2009).
52. M. Calcagnotto, D. Ponge, E. Demir, and D. Raabe, *Mater. Sci. Eng. A* 527, 2738 (2010).
53. J.H. Ryu, D.-I. Kim, H.S. Kim, H.K.D.H. Bhadeshia, and D.-W. Suh, *Scr. Mater.* 63, 297 (2010).
54. Q. Furnémont, G. Lacroix, S. Godet, K.T. Conlon, and P.J. Jacques, *Can. Metall. Q.* 43(1), 35–42 (2004).
55. J. Jung, H. Kim, and B. De Cooman, *ISIJ Int.* 50, 620 (2010).
56. S. Wronski, J. Tarasiuk, B. Bacroix, A. Baczanski, and C. Braham, *Mater. Charact.* 73, 52 (2012).
57. K. Yan, K.-D. Liss, I.B. Timokhina, and E.V. Pereloma, *Mater. Sci. Eng. A* 662, 185 (2016).
58. E. Jimenez-Melero, N. Van Dijk, L. Zhao, J. Sietsma, S. Offerman, J. Wright, and S. Van der Zwaag, *Acta Mater.* 55, 6713 (2007).
59. S.V. Radcliffe, and M. Schatz, *Acta Metall.* 10, 201 (1962).
60. I. Tsukatani, S. Hashimoto, and T. Inoue, *ISIJ Int.* 31, 992 (1991).

**Publisher's Note** Springer Nature remains neutral with regard to jurisdictional claims in published maps and institutional affiliations.